ACS APPLIED MATERIALS & INTERFACES
Research Article
www.acsami.org

Hydrothermal Synthesis of $CaIn_2S_4$-Reduced Graphene Oxide Nanocomposites with Increased Photocatalytic Performance

Jianjun Ding,*[†,‡] Wenhao Yan,[†,‡] Song Sun,[†,‡] Jun Bao,*[†,‡] and Chen Gao[†,‡]

[†]National Synchrotron Radiation Laboratory and Collaborative Innovation Center of Chemistry for Energy Materials, University of Science and Technology of China, Hefei, Anhui 230029, China

[‡]CAS Key Laboratory of Materials for Energy Conversion, Department of Materials Science and Engineering, University of Science and Technology of China, Hefei, Anhui 230026, China

S *Supporting Information*

ABSTRACT: A series of $CaIn_2S_4$-reduced graphene oxide (RGO) nanocomposites with different RGO contents were fabricated using a facile hydrothermal approach. During the hydrothermal process, the reduction of graphene oxide to RGO, in situ deposition of synthesized $CaIn_2S_4$ nanoparticles on RGO nanosheets and formation of chemical-bonding $CaIn_2S_4$-RGO nanocomposites were performed simultaneously. Under visible light irradiation, the as-prepared $CaIn_2S_4$-RGO nanocomposites showed enhanced photocatalytic performance for rhodamine B degradation and phenol oxidation. The sample with 5 wt % RGO hybridized $CaIn_2S_4$ exhibited the highest photocatalytic activity. The enhancement of photocatalytic performance may be related to the increased adsorption/reaction sites, positive shift of the valence band potential, and high separation efficiency of photogenerated charge carriers due to the electronic interaction between $CaIn_2S_4$ and RGO. We hope that this work can not only provide an in-depth study on the photocatalytic mechanism of RGO-enhanced activity, but also provide some insights for fabricating efficient and stable RGO-based photocatalysts in the potential applications of purifying polluted water resources.

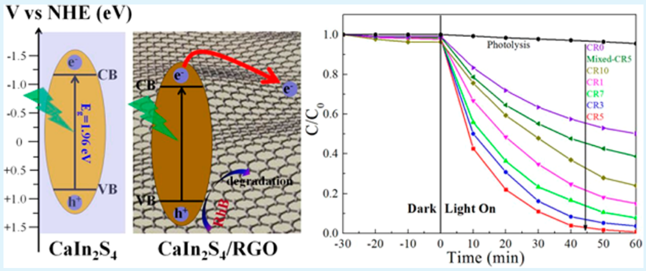

KEYWORDS: *$CaIn_2S_4$, reduced graphene oxide, nanocomposites, hydrothermal, visible-light photocatalysis*

INTRODUCTION

In past decades, photocatalysis has attracted a great deal of attention because of its potential application in the field of pollutant degradation and energy conversion. Since visible light accounts for about 43% of the incoming solar spectrum, developing visible-light-driven photocatalysts becomes important for the efficient utilization of the solar energy. Among a variety of visible photocatalysts, metal sulfides have been widely studied for their narrow band gaps and relatively negative potentials of the valence band compared to metal oxides. For example, CdS has been proven to be an effective photocatalyst though it suffers from chemical instability during the photocatalytic reaction.[1−3] Ternary metal sulfides, such as $ZnIn_2S_4$[4−6] and $CdIn_2S_4$,[7,8] have also been considered as candidate photocatalysts due to their narrow band gap with considerable chemical stability. However, as a single component, the low separation efficiency of photogenerated charge carriers has limited their large-scale practical application.

To address this issue, numerous efforts have been carried out on the development of composite photocatalysts with two or more components, as the separation efficiency of photogenerated charge carriers can been effectively suppressed at the interface of the composites. In recent years, graphene has aroused intense scientific interest for fabrication of graphene-based composite photocatalysts for enhanced performance because of its special two-dimensional structure, high surface area, and excellent electrical conductivity.[9] As an excellent supporting matrix, graphene can efficiently suppress the agglomeration of semiconductor particles, facilitate the charge separation and transportation from photocatalyst to graphene, and thereby improve the photocatalytic performance of photocatalysts. In most cases, graphene-based composites are prepared using graphene oxide as the precursor followed by its chemical reduction to reduced graphene oxide (RGO).To date, there are a lot of reports on RGO-based composites and their enhanced photocatalytic activity in hydrogen production or environmental application.[10−20] However, to the best of our knowledge, few studies have focused on the mechanism of RGO-enhanced performance from the point of view of the electronic energy band structure in RGO−semiconductor composites.

Our recent study found that ternary cubic $CaIn_2S_4$, first synthesized using a facile hydrothermal method, can produce hydrogen from pure water without any cocatalysts under visible light irradiation.[21] In this study, $CaIn_2S_4$-RGO nanocomposite with a strong coupling interface was prepared by a one-step

Received: May 8, 2014
Accepted: July 7, 2014
Published: July 7, 2014

dx.doi.org/10.1021/am5028296 | *ACS Appl. Mater. Interfaces* 2014, 6, 12877−12884

hydrothermal method for environmental remediation. Graphene oxide (GO), a lamellar two-dimensional material with unoxidized aromatic regions and aliphatic regions containing oxygen functional groups, was used as the precursor to synthesize RGO. During the hydrothermal process, the reduction of graphene oxide (GO) to RGO, in situ deposition of synthesized $CaIn_2S_4$ nanoparticles on the RGO nanosheets, and formation of chemical-bonding $CaIn_2S_4$-RGO nanocomposites can be achieved simultaneously. The nanocomposites exhibit increased photocatalytic performance for rhodamine B (RhB) degradation and phenol oxidation, compared to pure $CaIn_2S_4$ or a physical mixture of $CaIn_2S_4$/RGO under visible light irradiation. The introduction of RGO in $CaIn_2S_4$-RGO nanocomposites can not only increase the surface area and suppress the recombination of photogenerated charge carriers, but also change the electronic structure of $CaIn_2S_4$ by the chemical interaction between RGO and $CaIn_2S_4$, both of which could improve the photocatalytic activity. Furthermore, the $CaIn_2S_4$-RGO nanocomposites show good chemical and photocatalytic stability.

■ EXPERIMENTAL SECTION

Materials Preparation. Indium nitrate was purchased from Aladdin Industrial Inc. Natural graphite powder, calcium nitrate, and Thioacetamide were supplied by Sinopharm Chemical Reagent Co., Ltd. Deionized (DI) water was used in all experiments. All other reagents are at least of analytic reagent grade and used without further purification. Graphene oxide (GO) was prepared from natural graphite powder using a modified Hummers' method according to previous reports.[22]

The synthesis procedures of the $CaIn_2S_4$-RGO nanocomposites were based on a one-step hydrothermal method. In detail, a certain amount of GO was dispersed in 80 mL DI water by ultrasonication to obtain a homogeneous suspension. Then, 1.18 g $Ca(NO_3)_2 \cdot 4H_2O$ (5 mmol), 3.0 g $In(NO_3)_3$ (10 mmol), and 3.0 g CH_3CSNH_2 (40 mmol, double amount) were added into the suspension. The mixture was stirred for 30 min and then transferred to a 100 mL Teflon-lined stainless steel autoclave. A hydrothermal reaction took place in the sealed autoclave at 120 °C for 24 h. During the hydrothermal reaction, the reduction of GO was achieved with in situ deposition of $CaIn_2S_4$ nanoparticles on the reduced graphene oxide (RGO) substrate simultaneously. After that, the product was collected and washed using absolute ethanol and DI water several times before drying at 80 °C. The samples with different contents of GO to $CaIn_2S_4$ (1, 3, 5, 7, and 10 wt %) were labeled as CR1, CR3, CR5, CR7, and CR10, respectively.

For comparison, pure $CaIn_2S_4$ (CR0) or RGO was also prepared through a similar procedure in the absence of RGO or $CaIn_2S_4$ precursor. The mixed-$CaIn_2S_4$/RGO (Mixed-CR5, 5 wt % RGO) was synthesized by physical mixing of pure $CaIn_2S_4$ and RGO (5 wt %), with the same composition as that in the CR5 nanocomposite.

$CaIn_2S_4$-RGO and $CaIn_2S_4$ electrodes were prepared by a dip-coating method. Typically, 15 mg of powder was suspended in 50 mL absolute ethanol by ultrasonication to get a suspension, and then the suspension was dip-coated onto a 1 cm × 2 cm indium−tin oxide (ITO) glass electrode placed on a 70 °C heating station. After the elimination of ethanol, the dip-coating process was repeated ten times to obtain the final electrodes.

Characterization. Powder X-ray diffraction (XRD) patterns were measured using a Rigaku TTR III diffractometer with $Cu_{K\alpha}$ radiation ($\lambda = 0.15418$ nm) at a scan rate of 5° min^{-1} to determine the crystal phase of the prepared samples. The morphology and microstructure of the samples were investigated by a transmission electron microscopy (JEM-2100F) and a scanning electron microscopy (Sirion 200). Nitrogen adsorption−desorption isotherms were recorded on a Micromeritics ASAP 2020 M+C accelerated surface area and porosimetry system at 77 K. The surface areas were estimated using the Brunauer−Emmett−Teller (BET) method. The UV/vis diffuse reflectance spectrum of photocatalysts and absorption spectrum of RhB solution were measured at room temperature using a UV/vis spectrometer (SolidSpec-3700, Shimadzu, Japan). The surface characterization was carried out using X-ray Photoelectron Spectroscope (XPS, ESCALAB 250, Thermo-VG Scientific) with a base pressure lower than 1.0×10^{-10} Pa and $Mg_{K\alpha}$ radiation ($E = 1253.6$ eV) operated at 150 W as the X-ray source. Raman spectra were recorded with an InVia microscopic confocal Raman spectrometer using a 514.5 nm laser beam. Fourier transform infrared (FTIR) spectroscope was carried out on a Nicolet 8700 FTIR in a KBr pellet scanning from 4000 to 400 cm^{-1}. The photoelectrochemical properties were measured on a CHI-760D electrochemical analyzer in a standard three-electrode system using the prepared samples with an active area of ca. 1 cm^2 as the working electrodes, a platinum wire as the counter electrode, and Ag/AgCl as the reference electrode. KCl (1 M, pH = 7) solution was used as the electrolyte.

Photocatalytic Experiments. The photocatalytic activities of the $CaIn_2S_4$-RGO nanocomposites for RhB decomposition were evaluated. In the case of visible light irradiation, a 300 W Xe arc lamp (PLS-SXE 300, ChangTuo Ltd.) was used as the light source through infrared and UV cutoff filters to ensure visible illumination only (420 nm $\leq \lambda \leq$ 750 nm). In a typical experiment, 100 mg of photocatalyst was suspended in 120 mL of RhB solution ($(60-120) \times 10^{-6}$ mol/L) or phenol solution (20 mg/L) in a Pyrex glass cell. The distance between the lamp and the suspension surface was 20 cm. To eliminate the thermal effect during the photocatalytic reaction, a water jacket outside the Pyrex glass cell was used to keep the solution temperature constant at room temperature by flowing cooling water. Before the reaction, the prepared suspension was magnetically stirred for 30 min in the dark to ensure the establishment of an adsorption−desorption equilibrium between photocatalyst powders and RhB/phenol molecules. At given time intervals, the concentration changes of RhB/phenol were monitored by measuring the maximum absorption band (665 nm for RhB and 270 nm for phenol) in the UV−vis spectrum of RhB or phenol using a portable fiber spectrometer (SD2000, Ocean Optics). For comparison, the self-degradation of RhB (namely, photolysis) was also tested under similar conditions in the absence of photocatalysts.

■ RESULTS AND DISCUSSION

Structure and Morphology. Figure 1 shows the XRD patterns of $CaIn_2S_4$ and $CaIn_2S_4$-RGO nanocomposites. In general, no obvious difference in XRD patterns was observed among all the samples. The main diffraction peaks of all the samples at 27.4°, 28.4°, 33.1°, 43.4°, and 47.7°, correspond to the diffractions of the (311), (222), (400), (511), and (440) planes of cubic $CaIn_2S_4$ (PCPDF #310272), respectively. No other impurity peaks corresponding to binary sulfides or oxides

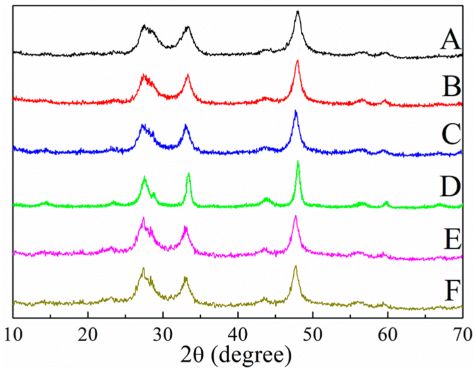

Figure 1. XRD patterns of the $CaIn_2S_4$-RGO nanocomposites: (A) CR0, (B) CR1, (C) CR3, (D) CR5, (E) CR7, and (F) CR10.

related to the reactants are detected, indicating the pure phase of cubic $CaIn_2S_4$. Furthermore, there is not any characteristic diffraction peaks for carbon species (GO or RGO) observed in the XRD patterns even though the content of GO is as high as 10 wt %, mainly due to its relatively low diffraction intensity and high dispersion.[23,24]

The morphology of $CaIn_2S_4$ and $CaIn_2S_4$-RGO nanocomposites was characterized by TEM and SEM. A mixture of differently shaped nanoparticles, including nanorods and nanosheets, is observed in Figure 2A. From the typical TEM/SEM images of CR5 nanocomposite (the highest photocatalytic activity for RhB degradation) in Figure 2B−C and Supporting Information Figure S1, it is found that the $CaIn_2S_4$ nanoparticles are very thin and look transparent, and they are dispersed on RGO sheets with good contact. This contact makes the interfacial charge transfer available at the interface of the composites. RGO displays a two-dimensional sheet with chiffon-like ripples and wrinkles resulting from the deformation and distortion of graphite sheets during the oxidation process. A well-defined crystal structure of cubic $CaIn_2S_4$ in CR5 nanocomposite is evidenced from the HRTEM image (Figure 2D). Clear lattice-fringe intervals of 0.33, 0.31, and 0.27 nm correspond to the (311), (222), and (400) crystal plane of cubic $CaIn_2S_4$, respectively.

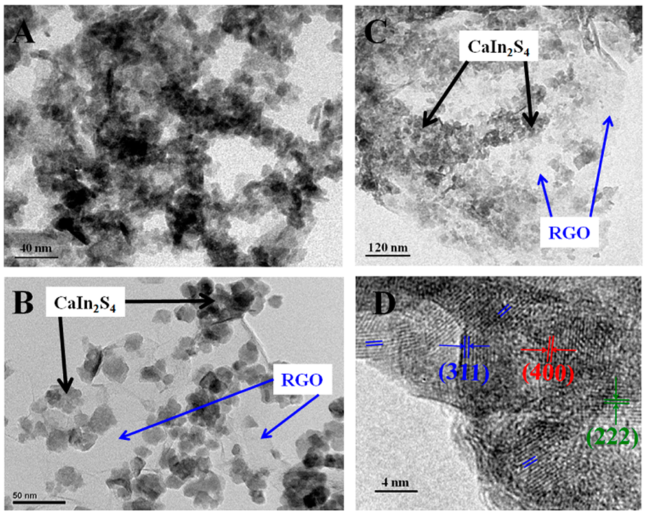

Figure 2. TEM images of $CaIn_2S_4$ (A) and CR5 nanocomposite (B−D).

To investigate the surface chemical composition and electronic state, XPS spectra of GO, RGO, and CR5 nanocomposite were collected. Characteristic binding energies of 346.7 and 350.1 eV for Ca^{2+} 2p, 445.1 and 452.6 eV for In^{3+} 3d, and 161.6 and 162.8 eV for S^{2-} 2p are observed for $CaIn_2S_4$ and CR5 nanocomposite, which are shown in Supporting Information Figure S2. In Figure 3A, the XPS spectrum of C 1s from GO can be deconvoluted into four small peaks which can be ascribed to the following functional groups: C—C (sp^2, 284.8 eV), C—O (epoxy/hydroxyl, 286.8 eV), C═O (carbonyl, 287.7 eV), and O—C═O (carboxyl, 289.5 eV).[25] After the hydrothermal reaction, the significant decrease of oxygen-containing functional groups is observed on the C 1s XPS spectra of RGO or CR5 nanocomposite (Figure 3B,C). The reduction degree of RGO can be calculated based on the XPS results.[26] It is found that the content of oxygen-containing carbon (including C—O, C═O, and O—C═O) decreased from 75.8% in GO to 25.8% in RGO after the hydrothermal reaction. These results indicate that most oxygen-containing functional groups can be efficiently removed through the hydrothermal reduction.

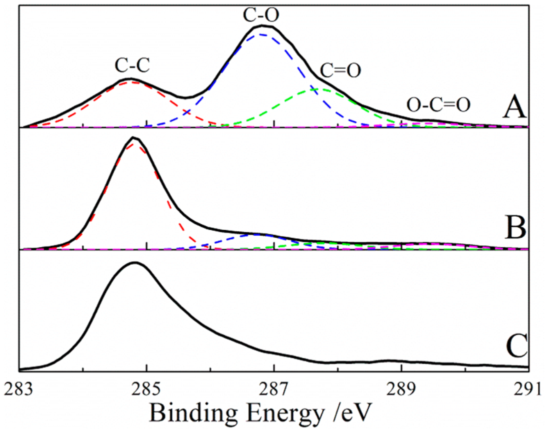

Figure 3. C 1s XPS spectra of GO (A), RGO (B), and CR5 (C) nanocomposite.

Further evidence for the reduction degree of oxygen functional groups comes from FTIR spectra of GO, RGO, and CR5 nanocomposite. For GO, the peaks at 845, 1056, 1222, 1398, and 1727 cm^{-1} correspond to the typical stretching of carbon−oxygen bonds. The peak at 1625 cm^{-1} may be assigned to the vibration of sp^2 hybridized C—C bonding, O—H bending vibration of epoxide group, or O—H deformation vibration of COOH group.[27−29] The broad absorption at 3000−3700 cm^{-1} corresponds to the stretching mode of −OH or the physically absorbed H_2O. After the hydrothermal reaction, only weak features appear and some peaks even vanish in the spectrum of RGO or CR5 nanocomposite, demonstrating the effective reduction of GO. Furthermore, a new absorption peak appeared at 1569 cm^{-1}, which may be attributed to the skeletal vibration of the graphene sheets.[11]

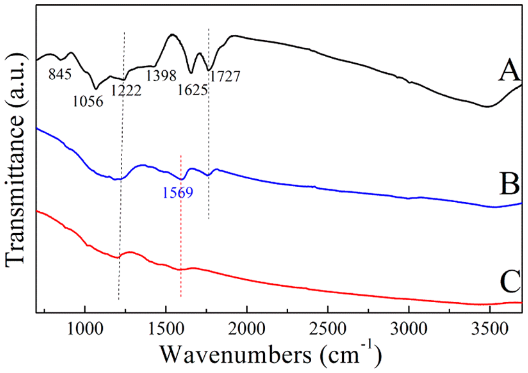

Figure 4. FTIR spectra of GO (A), RGO (B) and CR5 (C) nanocomposite.

Figure 5 shows the Raman spectra of GO, RGO, and $CaIn_2S_4$-RGO nanocomposites. In general, all the samples show characteristic peaks at about 1360 and 1590 cm^{-1}, corresponding to the D and G bands of graphene, respectively. The intensity ratio I_D/I_G over RGO or $CaIn_2S_4$-RGO nanocomposites is much higher than that of GO (0.86), which is typically observed when graphene is produced by reducing GO.[30,31] The result further demonstrates the reduction of GO

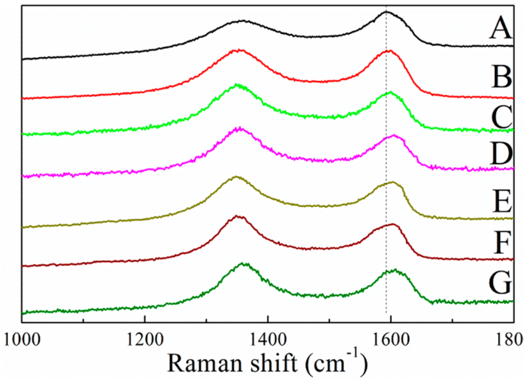

Figure 5. Raman spectra of GO (A), RGO (B), CR1 (C), CR3 (D), CR5 (E), CR7 (F), and CR10 (G).

to RGO and is consistent with the XPS or FTIR data. Moreover, it can be seen that the peak of the G-band was red-shifted from 1593 cm^{-1} to longer wavelength for the $CaIn_2S_4$-RGO nanocomposites compared with GO. The red-shift of G band was mainly caused by the electronic interaction between $CaIn_2S_4$ and RGO nanosheets with a firm interface.[32,33]

Figure 6 gives the N_2 adsorption−desorption isotherms of pure $CaIn_2S_4$ and $CaIn_2S_4$-RGO nanocomposites. As shown, all the samples exhibit a type IV isotherm according to the IUPAC classification, indicating the mesoporous nature. However, with the increase in the content of RGO, the shape of the hysteresis loop is changed from type H3 to H2, indicating the formation of slit-type pore structure.[34] Accordingly, the BET surface area and pore volume are gradually increased with increasing RGO content, as listed in Table 1. Therefore, the incorporation of RGO has an obvious effect on the pore structure and surface area of $CaIn_2S_4$-RGO nanocomposites. As we know, larger surface area will provide more adsorption/reaction sites during the photocatalytic reaction, which can be beneficial for the improvement of the photocatalytic activity.

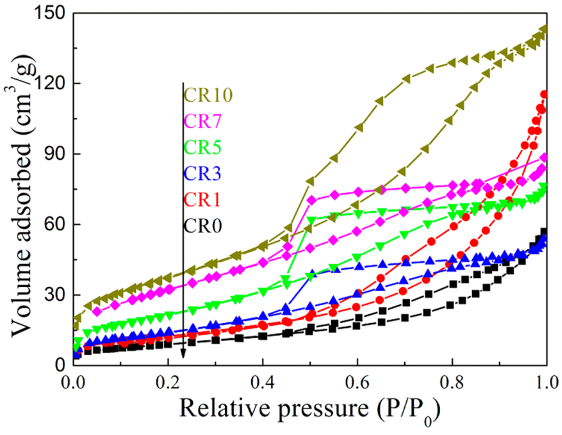

Figure 6. N_2 adsorption−desorption isotherms of $CaIn_2S_4$-RGO nanocomposites.

Figure 7 displays the UV−vis diffuse reflectance spectra of $CaIn_2S_4$-RGO nanocomposites. The cubic $CaIn_2S_4$ shows a wide absorption in visible region with an absorption edge end at about 575 nm, corresponding to the band gap of about 1.96 eV according to the Tauc equation. The enhancement of visible light absorption for $CaIn_2S_4$-RGO nanocomposites was mainly caused by the background absorption of RGO. However, the end of the absorption band-edge exhibits almost no change with increasing RGO content (Supporting Information Figure S3), which means that the introduction of RGO has little effect on the band gap value of $CaIn_2S_4$.

Table 1. Surface Area, Pore Volume, Flat-Band Potential, and Photocatalytic Reaction Rate Constant over $CaIn_2S_4$-RGO Nanocomposites

sample	RGO (wt %)	S_{BET} (m^2 g^{-1})	pore volume (cm^3 g^{-1})	flat-band potential[a] (V_{fb}, V)	rate constant[b] (k, min^{-1})
CR0	0	33.1	0.080	−1.06	0.0139
CR1	1.0	45.5	0.107	−0.93	0.0421
CR3	3.0	51.2	0.122	−0.89	0.0561
CR5	5.0	78.8	0.146	−0.85	0.0816
CR7	7.0	119.1	0.179	−0.81	0.0321
CR10	10.0	135.7	0.228	−0.75	0.0241

[a] Obtained from the x intercepts of the linear region in MS plots. [b] cat: 100 mg; RhB: 120 mL, 80 uM; $\lambda \geq 420$ nm; reaction time: 60 min.

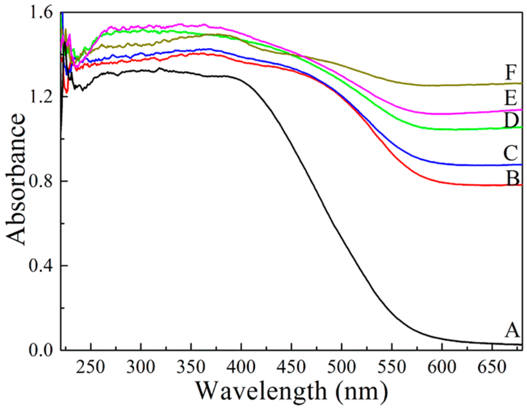

Figure 7. UV−visible diffuse reflectance spectra of the $CaIn_2S_4$-RGO nanocomposites: (A) CR0, (B) CR1, (C) CR3, (D) CR5, (E) CR7, and (F) CR10.

Photocatalytic Activity. To evaluate the photocatalytic activity of $CaIn_2S_4$-RGO nanocomposites under visible light irradiation, RhB was chosen as a model pollutant for photocatalytic degradation, which is a representative of organic dyes in textile effluents. From Figure 8, RhB had only about 5% self-degradation after irradiation for 60 min, which means the self-degradation effect of RhB was almost negligible under visible light irradiation. Adsorption of RhB on the photocatalyst reached an equilibrium state within 30 min in the dark. When $CaIn_2S_4$ nanoparticle was contained in the solution, the degradation of RhB increased to 49%, proving that $CaIn_2S_4$ was active for RhB photocatalytic degradation under visible light irradiation. However, it needs about 240 min to completely remove the RhB dye in the solution. Furthermore, it is found that the introduction of RGO can significantly enhance the photocatalytic activity of $CaIn_2S_4$. The optimal photocatalytic performance is observed when the RGO content reaches 5 wt %. Under 60 min visible light irradiation, the degradation of RhB for CR5 nanocomposite was measured to be about 99%. Its corresponding apparent first-order rate constant k is 0.0816 min^{-1}, which is about 5.9 times higher than that of pure $CaIn_2S_4$ (0.0139 min^{-1}), as listed in Table 1. It should be noted that the rate constant from mixed-CR5 composite was 0.0196 min^{-1}, which is much lower than that from the CR5 nanocomposite. The difference can be attributed

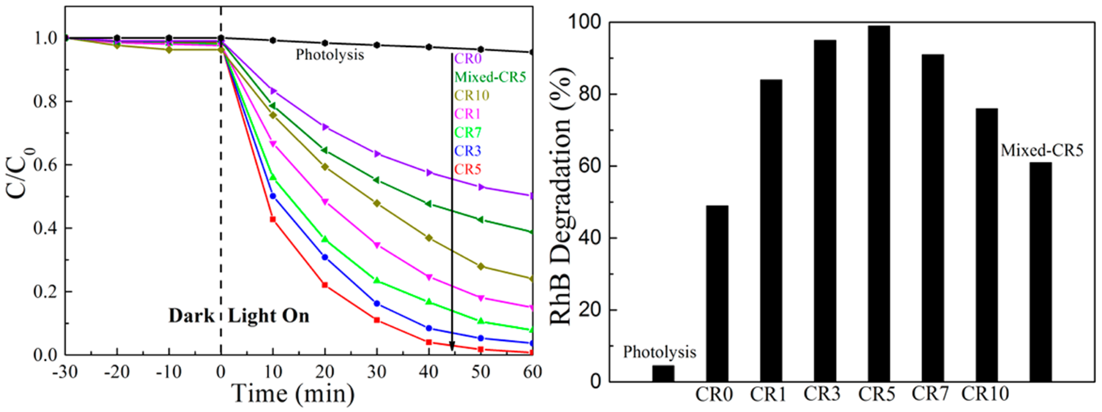

Figure 8. Degradation ratio of RhB solution (80 μM) after 60 min irradiation over photolysis, $CaIn_2S_4$-RGO nanocomposites, and mixed-CR5.

to the unique structure between $CaIn_2S_4$ and RGO. The chemical bonding between $CaIn_2S_4$ and RGO in $CaIn_2S_4$-RGO nanocomposites, demonstrated by the G-band red-shift of Raman peak, clearly reveals the formation of $CaIn_2S_4$-RGO nanocomposite with firm interfaces, which favors the interfacial charge transfer spatially available and accordingly improve the photocatalytic activity.

However, the photocatalytic activity over the $CaIn_2S_4$-RGO nanocomposites is decreased when the RGO content exceeds 5 wt %. In this case, the decrease may be attributed to the joint effect between the excellent charge transfer capability of RGO and its detrimental effect on visible light absorption.

The influence of the initial RhB concentration (C_0) on the photocatalytic rate over CR5 nanocomposite was also investigated, and the results are shown in Supporting Information Figure S4. By changing C_0 in the range 60−120 μM, the calculated rate constant was 0.115, 0.080, 0.0581, and 0.0425 min^{-1}, respectively. The photocatalytic rate of RhB becomes higher with decreasing the initial concentration, indicating that the initial concentration of RhB has a significant effect on the degradation rate. As we know, the degradation of RhB is de-ethylated initially, and then followed a destruction of the conjugated structure.[35,36] The inset of Supporting Information Figure S3 shows the temporal absorption spectra of RhB solution with an initial concentration of 80 μM. In general, the position of the absorption peak was shifted to shorter wavelength and the intensity of the peak was reduced with increasing irradiation time. After 60 min reaction, all the absorption peaks of RhB disappeared and no new peak was observed, indicating a complete degradation through photocatalytic reaction.

The stability of the CR5 nanocomposite was also demonstrated by five successive recycling experiments. As shown in Figure 9, after five consecutive reaction runs, the degradation of RhB still remained to 91% under 60 min visible light irradiation. The slight decrease in activity might be attributed to the fact that a large number of intermediates were formed and adsorbed on the surface of photocatalyst.[37] The structure and composition after the reaction were analyzed by XRD and XPS (Supporting Information Figures S5 and S6), which indicated no change in the structure and composition of CR5 nanocomposite. Therefore, the as-prepared $CaIn_2S_4$-RGO nanocomposites can be used as novel visible-light-driven photocatalysts with good stability.

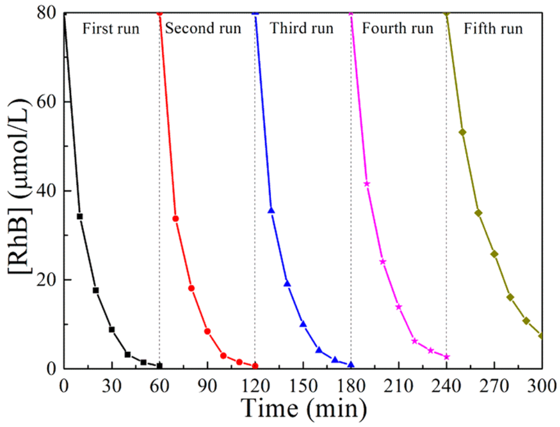

Figure 9. Stability of photocatalytic degradation of RhB for CR5 nanocomposite under visible light irradiation.

In addition, the photocatalytic performance for phenol oxidation was also evaluated as the photosensitization effect of phenol was negligible under visible light. Supporting Information Figure S7 shows the phenol removal rate against irradiation time over the $CaIn_2S_4$-RGO nanocomposites. The initial concentration of phenol was 20 mg/L. Similar to the photocatalytic performance for RhB degradation, the activities of phenol photo-oxidation for $CaIn_2S_4$-RGO nanocomposites were remarkably improved compared to pure $CaIn_2S_4$ or mixed-CR5 composite. The phenol removal rate over the CR5 nanocomposite reaches about 54.6% after 60 min irradiation, while the degraded phenol by pure $CaIn_2S_4$ was only 24.6%.

Origins of Enhanced Photocatalytic Performance. The photocatalytic reaction mainly includes the following three processes: (1) electron−hole pairs are generated inside the semiconductor with photo energy equal to or larger than the band gap of the semiconductor, (2) the photogenerated charge carriers separate and migrate to the surface of the semiconductor before recombination, and (3) a redox reaction takes place. Therefore, the electronic energy band structure of a photocatalyst directly affects its photocatalytic activity. To understand the origins of the enhanced photocatalytic performance for the $CaIn_2S_4$-RGO nanocomposites, Mott−Schottky (MS) and transient photocurrent measurement were performed through photoelectrochemical experiments.

Figure 10 shows the MS plots of the electrodes based on $CaIn_2S_4$ and $CaIn_2S_4$-RGO nanocomposites. Positive slope from the MS plot proves that $CaIn_2S_4$ is an n-type semiconductor.

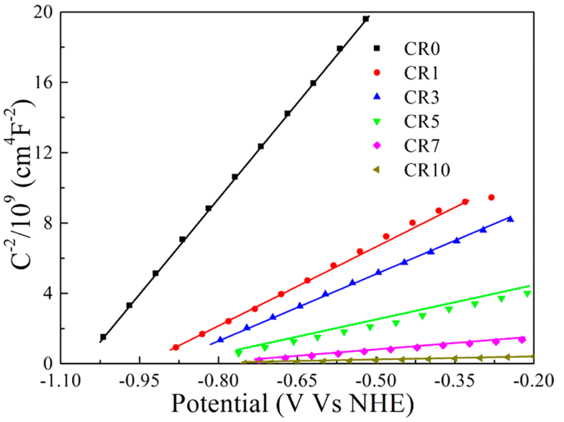

Figure 10. Mott−Schottky plots of $CaIn_2S_4$-RGO nanocomposites at the frequency of 1000 Hz.

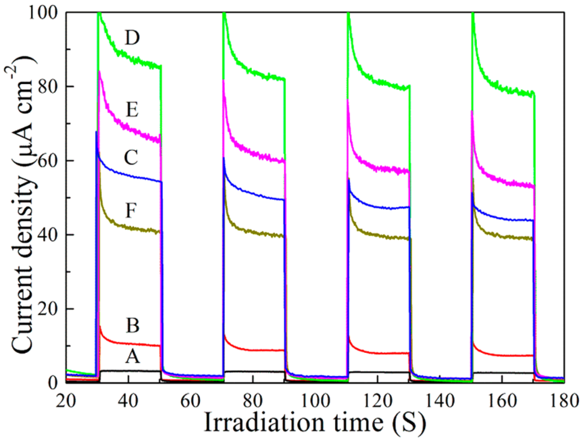

Figure 11. Transient photocurrent density responses of $CaIn_2S_4$-RGO nanocomposites with light on/off cycles under visible light irradiation: (A) CR0, (B) CR1, (C) CR3, (D) CR5, (E) CR7, and (F) CR10.

Compared to pure $CaIn_2S_4$, the slope of the $CaIn_2S_4$-RGO nanocomposites decreases to a lower value with increasing the RGO content, indicating higher donor density for the $CaIn_2S_4$-RGO nanocomposites.[38] The flat-band potential (V_{fb}), calculated from the x intercept of the linear region, is listed in Table 1. The V_{fb} of $CaIn_2S_4$-RGO nanocomposites shows a positive shift as compared with that of pure $CaIn_2S_4$. The reason may be attributed to the electronic interaction between RGO and $CaIn_2S_4$ in $CaIn_2S_4$-RGO nanocomposites that results in a shift of the Fermi level, which is consistent with the Raman shift of the above-mentioned G band. A similar phenomenon was also reported by Zhu in ZnO/graphene composite,[39] while negative shift of V_{fb} was found in Bi_2WO_6/graphene composite.[32,40]

It is well-known that the conduction band potential (or the Fermi level) of n-type semiconductor is very close (about 0−0.1 V more negative) to V_{fb},[41,42] so it can be deduced that the conduction band potential of $CaIn_2S_4$-RGO nanocomposites is more positive compared to $CaIn_2S_4$. As the band gap of $CaIn_2S_4$ was not changed after the introduction of RGO according to Figure 7, we can further speculate that the valence band potential of $CaIn_2S_4$-RGO nanocomposites is also more positive than that of $CaIn_2S_4$. Further evidence for the positive-shift of the valence band comes from valence band XPS.[43] In Supporting Information Figure S8, The position of the valence band maximum of $CaIn_2S_4$ and CR5 nanocomposite was calculated to be about 0.88 and 1.13 eV, respectively. Therefore, the oxidation capacity of the holes generated on the valence band of $CaIn_2S_4$-RGO nanocomposites will be higher than that of $CaIn_2S_4$. Supporting Information Figure S9 shows the photocatalytic degradation of RhB with the addition of holes and hydroxyl radicals' scavengers, respectively. The addition of *tert*-butanol as the hydroxyl radicals' scavengers only causes a slight decrease in RhB photodegradation, while the RhB can be hardly degraded with the addition of sacrificial reagent for holes (ammonium acetate, 10 mM). That is the reason the $CaIn_2S_4$-RGO nanocomposites exhibit higher photocatalytic activity for RhB degradation than pure $CaIn_2S_4$, because direct hole oxidation is the major reaction process in the photocatalytic degradation of RhB.[44,45]

To further study the charge transfer properties, the transient photocurrent responses were measured. Figure 11 shows the current−voltage curves for $CaIn_2S_4$ and $CaIn_2S_4$-RGO nanocomposites. It can be seen that uniform and reproducible photocurrent responses are observed over all electrodes, which indicates that the photocurrent response is reversible and the electrodes are stable. Why did the shapes of photocurrent curves of $CaIn_2S_4$ and RGO-modified $CaIn_2S_4$ have an obvious difference? This is due to the fact that the photogenerated electrons transfer from the conduction band of $CaIn_2S_4$ to RGO nanosheets at the interface of the nanocomposites. From Figure 11, the pure $CaIn_2S_4$ electrode exhibits weak photocurrent density (3.4 μA cm^{-2}). Obviously, significant enhancement of photocurrent density for $CaIn_2S_4$-RGO electrodes was observed. When the RGO content was increased from 1 wt % to 5 wt %, the photocurrent density increased from 10.6 to 88.5 μA cm^{-2}. The highest photocurrent density for the CR5 nanocomposite is about 26 times higher than that of the pure $CaIn_2S_4$ electrode, indicating efficient separation of photogenerated charge carriers in the composite. However, reduced photocurrent density was observed once the RGO content exceeded 5 wt %, probably due to intense light scattering and absorbance of RGO, but they still maintain better photocurrent responses than that of pure $CaIn_2S_4$. A similar phenomenon was also confirmed by the typical electrochemical impedance spectra (EIS, Supporting Information Figure S10). For $CaIn_2S_4$-RGO nanocomposites, the semicircle in the plot was much shorter compared to the pure $CaIn_2S_4$. The CR5 nanocomposite shows the smallest semicircle among all the $CaIn_2S_4$-RGO nanocomposites, indicating efficient charge transfer and superior electronic conductivity. All these results demonstrate that RGO can function as an effective cocatalyst in the $CaIn_2S_4$-RGO nanocomposites to effectively suppress the charge recombination and therefore improve the photocatalytic performance.

On the basis of the results of photodegradation and photoelectrochemical experiments, a mechanism for increased photocatalytic performance over the $CaIn_2S_4$-RGO nanocomposites is proposed in Figure 12. Under visible light irradiation, electron−hole pairs are generated on the conduction band and valence band of $CaIn_2S_4$. Since the Fermi level of graphene (−0.08 V vs NHE[46]) is more positive than the conduction-band potential of $CaIn_2S_4$, the photogenerated electrons can transfer readily from the conduction band of $CaIn_2S_4$ to RGO nanosheets. As a result, the separation efficiency of photogenerated charge carriers can be effectively improved at the interface of the nanocomposites, which

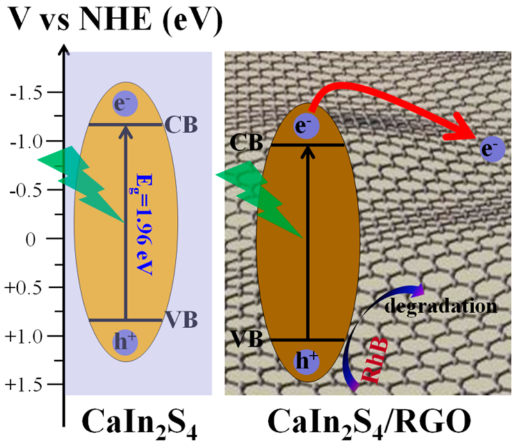

Figure 12. Energy band diagram and photocatalytic mechanism of $CaIn_2S_4$ and $CaIn_2S_4$-RGO nanocomposites.

provides more hole participation in the photocatalytic reaction. Meanwhile, the introduction of RGO can positively shift the valence band potential of $CaIn_2S_4$ to a higher value, which can improve the oxidation capability of the photogenerated holes in the valence band and thereby enhance the photocatalytic performance for RhB degradation..

■ CONCLUSIONS

In summary, for the first time, a series of $CaIn_2S_4$-RGO nanocomposites were synthesized using one-step hydrothermal method, where the reduction of GO to RGO was achieved with in situ deposition of $CaIn_2S_4$ nanoparticles on the RGO nanosheets simultaneously. As reported here, the as-prepared $CaIn_2S_4$-RGO nanocomposites provide more adsorption and reaction sites, positively shift the position of the valence band potential and improve charge transportation and separation efficiency. On the basis of these advantages, the $CaIn_2S_4$-RGO nanocomposites exhibit increased photocatalytic performance for RhB degradation and phenol oxidation under visible light irradiation, which is much higher than that of pure $CaIn_2S_4$ or physical mixture of $CaIn_2S_4$/RGO. It is hoped that our work can open new insights for the design and synthesis of other RGO-based nanocomposites with efficient performance in purifying polluted water resources.

■ ASSOCIATED CONTENT

Ⓢ Supporting Information

SEM images, XPS spectra of $CaIn_2S_4$ and CR5 nanocomposite, UV−visible diffuse reflectance spectra, degradation curves under different initial concentrations of RhB solution over CR5 nanocomposite, XRD pattern of CR5 nanocomposite after photocatalytic reaction, XPS spectra of CR5 nanocomposite after photocatalytic reaction, photocatalytic performance for phenol oxidation, VB XPS spectra, photocatalytic degradation of RhB (80 μM) with the addition of hole and radical scavengers over CR5 nanocomposite, EIS Nyquist impedance plots. This material is available free of charge via the Internet at http://pubs.acs.org.

■ AUTHOR INFORMATION

Corresponding Authors

*Tel: (+86)551-63607492. Fax: (+86)551-65141078. E-mail: dingjj@ustc.edu.cn.
*E-mail: baoj@ustc.edu.cn.

Notes

The authors declare no competing financial interest.

■ ACKNOWLEDGMENTS

This work was supported by National Basic Research Program of China (973 Program) (2012CB922004), Anhui Provincial Natural Science Foundation (1308085MB27), and National Nature Science Foundation of China (11179034, 11205159).

■ REFERENCES

(1) Jing, D. W.; Guo, L. J. A Novel Method for the Preparation of a Highly Stable and Active CdS Photocatalyst with a Special Surface Nanostructure. *J. Phys. Chem. B* **2006**, *110*, 11139−11145.

(2) Bao, N. Z.; Shen, L. M.; Takata, T.; Domen, K. Self-Templated Synthesis of Nanoporous CdS Nanostructures for Highly Efficient Photocatalytic Hydrogen Production under Visible Light. *Chem. Mater.* **2008**, *20*, 110−117.

(3) Zhang, K.; Guo, L. J. Metal Sulphide Semiconductors for Photocatalytic Hydrogen Production. *Catal. Sci. Technol.* **2013**, *3*, 1672−1690.

(4) Lei, Z. B.; You, W. S.; Liu, M. Y.; Zhou, G. H.; Takata, T.; Hara, M.; Domen, K.; Li, C. Photocatalytic Water Reduction under Visible Light on a Novel $ZnIn_2S_4$ Catalyst Synthesized by Hydrothermal Method. *Chem. Commun.* **2003**, *17*, 2142−2143.

(5) Shen, S. H.; Zhao, L.; Guo, L. J. Cetyltrimethylammoniumbromide (CTAB)-Assisted Hydrothermal Synthesis of $ZnIn_2S_4$ as an Efficient Visible-Light-Driven Photocatalyst for Hydrogen Production. *Int. J. Hydrogen Energy* **2008**, *33*, 4501−4510.

(6) Chen, Y. J.; Huang, R. K.; Chen, D. Q.; Wang, Y. S.; Liu, W. J.; Li, X. N.; Li, Z. H. Exploring the Different Photocatalytic Performance for Dye Degradations over Hexagonal $ZnIn_2S_4$ Microspheres and Cubic $ZnIn_2S_4$ Nanoparticles. *ACS Appl. Mater. Interfaces* **2012**, *4*, 2273−2279.

(7) Kale, B. B.; Baeg, J.-O.; Lee, S. M.; Chang, H.; Moon, S.-J.; Lee, C. W. $CdIn_2S_4$ Nanotubes and "Marigold" Nanostructures: A Visible-Light Photocatalyst. *Adv. Funct. Mater.* **2006**, *16*, 1349−1354.

(8) Wang, W. J.; Ng, T. W.; Ho, W. K.; Huang, J. H.; Liang, S. J.; An, T. C.; Li, G. Y.; Yu, J. C.; Wong, P. K. $CdIn_2S_4$ Microsphere as an Efficient Visible-Light-Driven Photocatalyst for Bacterial Inactivation: Synthesis, Characterizations and Photocatalytic Inactivation Mechanisms. *Appl. Catal., B* **2013**, *129*, 482−490.

(9) Geim, A. K.; Novoselov, K. S. The Rise of Graphene. *Nat. Mater.* **2007**, *6*, 183−191.

(10) Williams, G.; Seger, B.; Kamat, P. V. TiO_2-Graphene Nanocomposites. UV-Assisted Photocatalytic Reduction of Graphene Oxide. *ACS Nano* **2008**, *2*, 1487−1491.

(11) Zhang, H.; Lv, X. J.; Li, Y. M.; Wang, Y.; Li, J. H. P25-Graphene Composite as a High Performance Photocatalyst. *ACS Nano* **2010**, *4*, 380−386.

(12) Zhang, X.-Y.; Li, H.-P.; Cui, X.-L.; Lin, Y. H. Graphene/TiO_2 Nanocomposites: Synthesis, Characterization and Application in Hydrogen Evolution from Water Photocatalytic Splitting. *J. Mater. Chem.* **2010**, *20*, 2801−2086.

(13) Li, Q.; Guo, B. D.; Yu, J. G.; Ran, J. R.; Zhang, B. H.; Yan, H. J.; Gong, J. R. Highly Efficient Visible-Light-Driven Photocatalytic Hydrogen Production of CdS-Cluster-Decorated Graphene Nanosheets. *J. Am. Chem. Soc.* **2011**, *133*, 10878−10884.

(14) Xie, G. C.; Zhang, K.; Guo, B. D.; Liu, Q.; Fang, L.; Gong, J. R. Graphene-Based Materials for Hydrogen Generation from Light-Driven Water Splitting. *Adv. Mater.* **2013**, *25*, 3820−3839.

(15) Ding, J. J.; Yan, W. H.; Xie, W.; Sun, S.; Bao, J.; Gao, C. Highly Efficient Photocatalytic Hydrogen Evolution of graphene/$YInO_3$ Nanocomposites under Visible Light Irradiation. *Nanoscale* **2014**, *6*, 2299−2306.

(16) Zhou, J.; Tian, G. H.; Chen, Y. J.; Meng, X. Y.; Shi, Y. H.; Cao, X. R.; Pan, K.; Fu, H. G. In situ Controlled Growth of $ZnIn_2S_4$ Nanosheets on Reduced Graphene Oxide for Enhanced Photocatalytic

Hydrogen Production Performance. *Chem. Commun.* **2013**, *49*, 2237−2239.

(17) Ye, L.; Fu, J. L.; Xu, Z.; Yuan, R. S.; Li, Z. H. Facile One-Pot Solvothermal Method to Synthesize Sheet-on-Sheet Reduced Graphene Oxide (RGO)/$ZnIn_2S_4$ Nanocomposite with Superior Photocatalytic Performance. *ACS Appl. Mater. Interfaces* **2014**, *6*, 3483−3490.

(18) Sreeprasad, T. S.; Maliyekkal, S. M.; Lisha, K. P.; Pradeep, T. Reduced Graphene Oxide-Metal/Metal Oxide Composites: Facile Synthesis and Application in Water Purification. *J. Hazard. Mater.* **2011**, *186*, 921−931.

(19) Sreeprasad, T. S.; Pradeep, T. Graphene for Environmental and Biological Applications. *Int. J. Mod. Phys. B* **2012**, *26*, 1242001.

(20) Upadhyay, R. K.; Soin, N.; Roy, S. S. Role of Graphene/Metal Oxide Composites as Photocatalysts, Adsorbents and Disinfectants in Water Treatment: a Review. *RSC Adv.* **2014**, *4*, 3823−3851.

(21) Ding, J. J.; Sun, S.; Yan, W. H.; Bao, J.; Gao, C. Photocatalytic H_2 Evolution on a Novel $CaIn_2S_4$ Photocatalyst under Visible Light Irradiation. *Int. J. Hydrogen Energy* **2013**, *38*, 13153−13158.

(22) Xu, Y. X.; Bai, H.; Lu, G. W.; Li, C.; Shi, G. Q. Flexible Graphene Films via the Filtration of Water-Soluble Noncovalent Functionalized Graphene Sheets. *J. Am. Chem. Soc.* **2008**, *130*, 5856−5857.

(23) Wang, W. G.; Yu, J. G.; Xiang, Q. J.; Cheng, B. Enhanced Photocatalytic Activity of Hierarchical Macro/mesoporous TiO_2−graphene Composites for Photodegradation of Acetone in Air. *Appl. Catal., B* **2012**, *119−120*, 109−116.

(24) Low, J. X.; Yu, J. G.; Li, Q.; Cheng, B. Enhanced Visible-Light Photocatalytic Activity of Plasmonic Ag and Graphene Co-Modified Bi_2WO_6 Nanosheets. *Phys. Chem. Chem. Phys.* **2014**, *16*, 1111−1120.

(25) Gu, L.; Wang, J. Y.; Cheng, H.; Zhao, Y. Z.; Liu, L. F.; Han, X. J. One-Step Preparation of Graphene-Supported Anatase TiO_2 with Exposed {001} Facets and Mechanism of Enhanced Photocatalytic Properties. *ACS Appl. Mater. Interfaces* **2013**, *5*, 3085−3093.

(26) Chen, Y. J.; Ge, H.; Wei, L.; Li, Z. H.; Yuan, R. S.; Liu, P.; Fu, X. Z. Reduction Degree of Reduced Graphene Oxide (RGO) Dependence of Photocatalytic Hydrogen Evolution Performance over RGO/$ZnIn_2S_4$ Nanocomposites. *Catal. Sci. Technol.* **2013**, *3*, 1712−1717.

(27) Fu, Y. S.; Wang, X. Magnetically Separable $ZnFe_2O_4$−Graphene Catalyst and Its High Photocatalytic Performance under Visible Light Irradiation. *Ind. Eng. Chem. Res.* **2011**, *50*, 7210−7218.

(28) Xiang, Q. J.; Yu, J. G.; Jaroniec, M. Preparation and Enhanced Visible-Light Photocatalytic H_2-Production Activity of Graphene/C_3N_4 Composites. *J. Phys. Chem. C* **2011**, *115*, 7355−7363.

(29) Shen, J. F.; Li, T.; Long, Y.; Shi, M.; Li, N.; Ye, M. X. One-Step Solid State Preparation of Reduced Graphene Oxide. *Carbon* **2012**, *50*, 2134−2140.

(30) Sher Shah, M. S.; Zhang, K.; Park, A. R.; Kim, K. S.; Park, N. G.; Park, J. H.; Yoo, P. J. Single-Step Solvothermal Synthesis of Mesoporous Ag-TiO_2-Reduced Graphene Oxide Ternary Composites with Enhanced Photocatalytic Activity. *Nanoscale* **2013**, *5*, 5093−5101.

(31) Xiang, Q. J.; Yu, J. G.; Jaroniec, M. Synergetic Effect of MoS_2 and Graphene as Cocatalysts for Enhanced Photocatalytic H_2 Production Activity of TiO_2 Nanoparticles. *J. Am. Chem. Soc.* **2012**, *134*, 6575−6578.

(32) Gao, E. P.; Wang, W. Z.; Shang, M.; Xu, J. H. Synthesis and Enhanced Photocatalytic Performance of Graphene-Bi_2WO_6 Composite. *Phys. Chem. Chem. Phys.* **2011**, *13*, 2887−2893.

(33) Manna, A. K.; Pati, S. K. Tuning the Electronic Structure of Graphene by Molecular Charge Transfer: A Computational Study. *Chem.—Asian J.* **2009**, *4*, 855−860.

(34) Dong, S. Y.; Sun, J. Y.; Li, Y. K.; Yu, C. F.; Li, Y. H.; Sun, J. H. $ZnSnO_3$ Hollow Nanospheres/reduced Graphene Oxide Nanocomposites as High-Performance Photocatalysts for Degradation of Metronidazole. *Appl. Catal., B* **2014**, *144*, 386−393.

(35) Zhao, W.; Chen, C. C.; Li, X. Z.; Zhao, J. C.; Hidaka, H.; Serpone, N. Photodegradation of Sulforhodamine-B Dye in Platinized Titania Dispersions under Visible Light Irradiation: Influence of Platinum as a Functional Co-Catalyst. *J. Phys. Chem. B* **2002**, *106*, 5022−5028.

(36) Fu, H. B.; Pan, C. S.; Yao, W. Q.; Zhu, Y. F. Visible-Light-Induced Degradation of Rhodamine B by Nanosized Bi_2WO_6. *J. Phys. Chem. B* **2005**, *109*, 22432−22439.

(37) Wang, P. F.; Ao, Y. H.; Wang, C.; Hou, J.; Qian, J. Enhanced Photoelectrocatalytic Activity for Dye Degradation by Graphene-Titania Composite Film Electrodes. *J. Hazard. Mater.* **2012**, *223−224*, 79−83.

(38) Luo, W. J.; Li, Z. S.; Jiang, X. J.; Yu, T.; Liu, L. F.; Chen, X. Y.; Ye, J. H.; Zou, Z. G. Correlation between the Band Positions of $(SrTiO_3)_{1-x}\cdot(LaTiO_2N)_x$ Solid Solutions and Photocatalytic Properties under Visible Light Irradiation. *Phys. Chem. Chem. Phys.* **2008**, *10*, 6717−6723.

(39) Xu, T. G.; Zhang, L. W.; Cheng, H. Y.; Zhu, Y. F. Significantly Enhanced Photocatalytic Performance of ZnO via Graphene Hybridization and the Mechanism Study. *Appl. Catal., B* **2011**, *101*, 382−387.

(40) Sun, Z. H.; Guo, J. J.; Zhu, S. M.; Mao, L.; Ma, J.; Zhang, D. A High-Performance Bi_2WO_6-Graphene Photocatalyst for Visible Light-Induced H_2 and O_2 Generation. *Nanoscale* **2014**, *6*, 2186−2193.

(41) Scaife, D. E. Oxide Semiconductors in Photoelectrochemical Conversion of Solar Energy. *Sol. Energy* **1980**, *25*, 41−54.

(42) Huang, H. J.; Li, D. Z.; Lin, Q.; Shao, Y.; Chen, W.; Hu, Y.; Chen, Y. B.; Fu, X. Z. Efficient Photocatalytic Activity of PZT/TiO_2 Heterojunction under Visible Light Irradiation. *J. Phys. Chem. C* **2009**, *113*, 14264−14269.

(43) Chen, X. B.; Liu, L.; Yu, P. Y.; Mao, S. S. Increasing Solar Absorption for Photocatalysis with Black Hydrogenated Titanium Dioxide Nanocrystals. *Science* **2011**, *331*, 746−750.

(44) Zhou, F.; Shi, R.; Zhu, Y. F. Significant Enhancement of the Visible Photocatalytic Degradation Performances of γ-Bi_2MoO_6 Nanoplate by Graphene Hybridization. *J. Mol. Catal. A: Chem.* **2011**, *340*, 77−82.

(45) Qamar, M.; Khan, A. Mesoporous Hierarchical Bismuth Tungstate as a Highly Efficient Visible-Light-Driven Photocatalyst. *RSC Adv.* **2014**, *4*, 9542−9550.

(46) Wang, X.; Zhi, L. J.; Mullen, K. Transparent, Conductive Graphene Electrodes for Dye-Sensitized Solar Cells. *Nano Lett.* **2008**, *8*, 323−327.